

RESEARCH

Open Access



Structural Responses of Reinforced Concrete Pile Foundations Subjected to Pressures from Compressed Air for Renewable Energy Storage

Dichuan Zhang*, Jong Kim, Saule Tulebekova, Dilmurat Saliyev and Deuckhang Lee

Abstract

A renewable energy storage system is being proposed through a multi-disciplinary research project. This system utilizes reinforced concrete pile foundations to store renewable energy generated from solar panels attached to building structures. The renewable energy can be stored in the form of compressed air inside the pile foundation with a hollowed section. The pile foundation should resist complex combined actions including structural loads, soil effects, and pressures induced from the compressed air, and thus it requires a careful analysis and design considerations to secure a sufficient structural safety. This paper presents analytical investigation results on the structural responses of the energy piles under these combined loadings. The pile foundations were designed based on the current design practices for various building geometries including the number of stories and column spacing. The magnitude of air pressure was determined from the thermodynamic cycles for the available renewable energy for storage considering building and pile foundation geometries. Finite element analyses were conducted using an elastic 3D model to determine critical tensile stresses of the pile foundation. These critical tensile stresses were used to identify required reinforcement in the pile section. On this basis, several nonlinear finite element analyses were then conducted using inelastic constitutive models of materials to investigate the crack patterns of the hollowed concrete section. Recommendations were finally presented for proper practical designs of the pile foundation serving as the renewable energy storage medium.

Keywords: reinforced concrete, pile foundation, structural responses, compressed air, renewable energy storage

1 Introduction

One of the effective ways of utilizing renewable energy is to supply electrical power timely for the daily operations of buildings, which is obtained directly from solar panels or wind mills attached to buildings (Hayter and Kandt 2011). However, the solar and wind energy have an intermittent nature that their availability significantly depends on climate and day-and-night diurnal cycles (Rugolo and Aziz 2012). This intermittent characteristic of the renewable energy requires efficient energy storage methods to timely

match the generated renewable energy with the demands of customers. Thus a new renewable energy storage system was developed through a multi-disciplinary research program (Sabirova et al. 2016; Tulebekova et al. 2017), and the main feature of this system is to utilize reinforced concrete (RC) pile foundations to store the renewable energy generated from solar panels attached to building structures. The renewable energy can be stored inside the RC pile foundation using the so-called compressed air energy storage (CAES) technology, termed here as CAES pile. The CAES is one of promising methods with high reliability, economic feasibility and low environmental impacts (Cavallo 2007; Lund and Salgi 2017). However, the applications of the CAES are quite limited in building structures due to the inherent difficulties in identifying reliable,

*Correspondence: dichuan.zhang@nu.edu.kz
Nazarbayev University, 53 Kabanbay Batyr Ave, Astana 010000, Republic of Kazakhstan
Journal information: ISSN 1976-0485 / eISSN 2234-1315

safe and cost-effective storage media (Zhang et al. 2012). Some application examples can be found in elsewhere (e.g. McIntosh plant in the US and Huntorf plant in Germany), which are currently adopted only in power plants with large underground caverns.

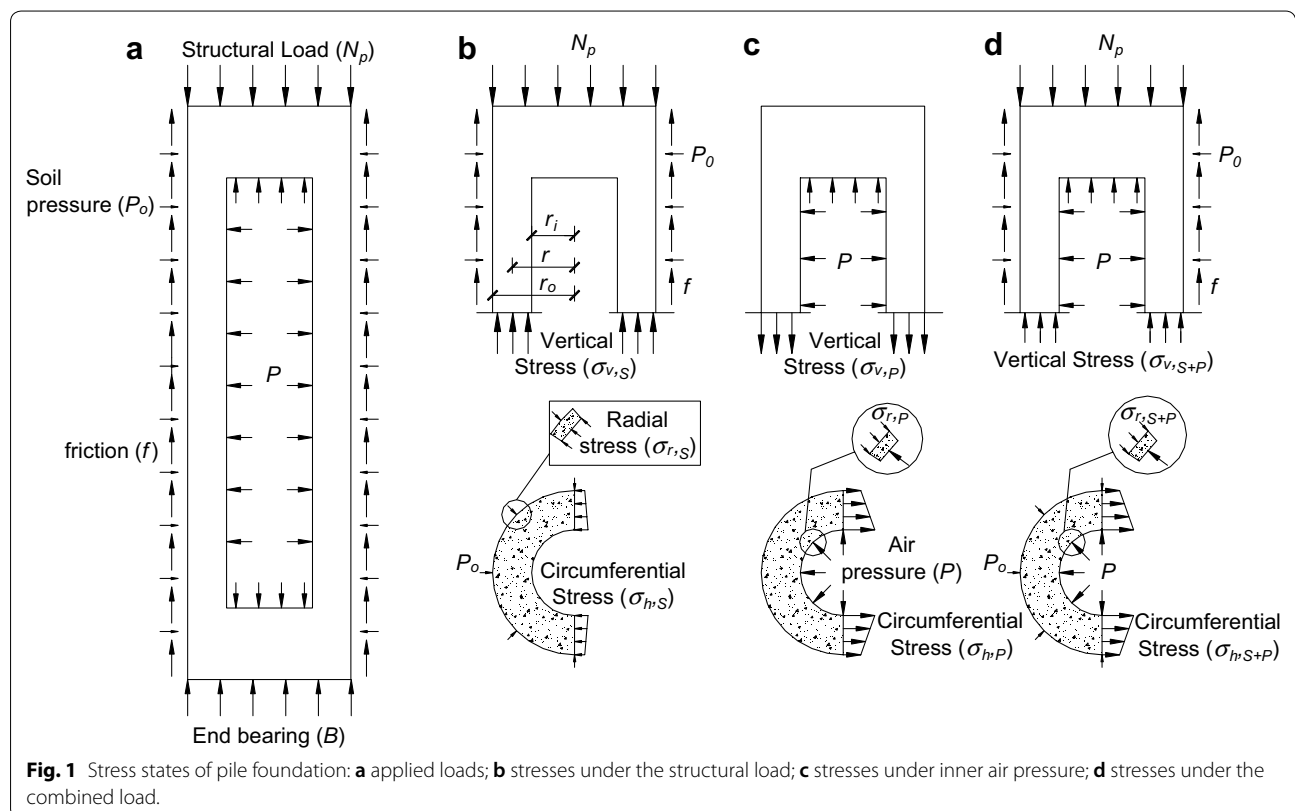
To overcome such a limitation, in this study, the RC pile foundation with a hollowed section was used as an energy storage tank, which results in the reduction of the effective cross-section area in the structural concrete pile. Moreover, in the pile foundation, more complex stress conditions are expected due to the combined loadings among structural loads from a super structure, soil effects and compressed-air pressures inside the pile. This paper presents analytical investigation results on the structural behaviors of the CAES pile under the combined loading through detailed finite element analyses. The pile foundation is designed based on the current design practices considering different building geometries, such as the number of stories and column spacing. The magnitude of compressed air pressure is determined from thermodynamic cycles in the CAES for the available renewable energy considering building and pile foundation geometries. The finite element analyses were conducted using an elastic 3D model to determine the critical tensile stresses induced in the pile

foundation, and these tensile stresses are used to determine the required amount of hoop reinforcements for proper crack control performances. Nonlinear finite element analyses are then conducted to investigate realistic cracking patterns in the concrete piles reinforced properly with the hoop reinforcements.

2 Background

2.1 Stress State in the Pile Foundation

The pile foundation is subjected to combined structural loads and inner air pressure. Figure 1 shows the stress states of the pile foundation. As shown in Fig. 1a, the pile is subjected to the structural load (N_p), soil boundary forces, which includes the shaft friction from soil (f), the end bearing (B), and the soil lateral pressure (P_o), and the air pressure applied on the inner surface of the pile (P). In the pile concrete section, internal resistances under the structural load including the vertical ($\sigma_{v,s}$), circumferential ($\sigma_{h,s}$) and radial ($\sigma_{r,s}$) stresses are developed, as shown in Fig. 1b. Under the vertical load, all these stresses introduce compression to the pile foundation. On the other hand, under the air pressure (P), the vertical ($\sigma_{v,p}$) and circumferential ($\sigma_{h,p}$) stresses induce tensile stresses to the sections of the pile foundation, while the radial stress ($\sigma_{r,p}$) causes compression (see Fig. 1c). When the



air pressure is much larger than the lateral soil pressure and vertical structural load, the combined load can cause the circumferential ($\sigma_{h,s+p}$) or even vertical ($\sigma_{v,s+p}$) tensile stresses (see Fig. 1d). These tensile stresses have potential to make concrete crack, and it can also result in the leakage of the air pressure or even the catastrophic failure of the pile foundation.

The similar circumferential tensile stresses were also observed in conical concrete tanks for liquid storages due to the hydrostatic pressures (Azabi 2014). The concrete tank is typically designed not to be cracked under the circumferential tensile stress according to ACI350 (2014). However, the compressed air pressure is expected to be much larger than the hydrostatic pressure (around 0.5 MPa) in the concrete tank, and thus it might not be practical to keep the concrete section uncracking in the CAES pile. Moreover, the concrete tank has much smaller wall thickness than the pile foundation, and the circumferential tensile stress distributions in the pile foundation are not uniform as observed in the thin-walled concrete tank. Therefore, it is possible that the tensile cracks might not penetrate the entire section of the pile foundation. The tensile stress distributions in elastic circular hollowed sections can be determined using the Lamé's Equations (Purushothama and Ramasamy 2010). On this basis, the circumferential tensile stress for the elastic thick-walled section under inner or outer pressure can be calculated, as follows:

$$\sigma_{h,p} = (Pr_i^2 - P_o r_o^2) / (r_o^2 - r_i^2) + (P - P_o)r_i^2 r_o^2 / (r_o^2 - r_i^2)r^2 \tag{1}$$

where r_i and r_o are the inner and outer radius, respectively, and r is the radius at the point of interest. This close-form solution can only predict the circumferential stress for linear elastic materials, and it will be used to compare with the finite element results described later in this paper.

2.2 Thermodynamic Cycles in CAES

One of the compressed air energy storage technologies uses an advanced-adiabatic process (Energy Storage Association 2018). This process includes four thermodynamic cycles including: (1) compression; (2) cooling; (3) heating; (4) expansion. The process is illustrated in Fig. 2.

2.2.1 Compression Process

The compression process can be identified using the energy conservation principle. For simplification purposes, the isentropic adiabatic compression condition is assumed, and the energy balance for the ideal diatomic gas can be expressed based on Al Shemmeri (2010), as follows:

$$w = 3.5nR(T_2 - T_1) \tag{2}$$

where w is the work done by the compressor (J), n is the amount of air passing through the compressor (mol), T is the absolute air temperature (K), R is the universal gas constant, and 8.31 J/mol. K was adopted in this study. T_1 is the ambient air temperature, and T_2 is the air temperature after the compression process. The electric power generated from the solar panel (\dot{w}_{in}) can be used to power the compressor based on the energy balance principal, as follows:

$$\dot{w}_{in} = 3.5\dot{n}R(T_2 - T_1)/\eta_1 \tag{3}$$

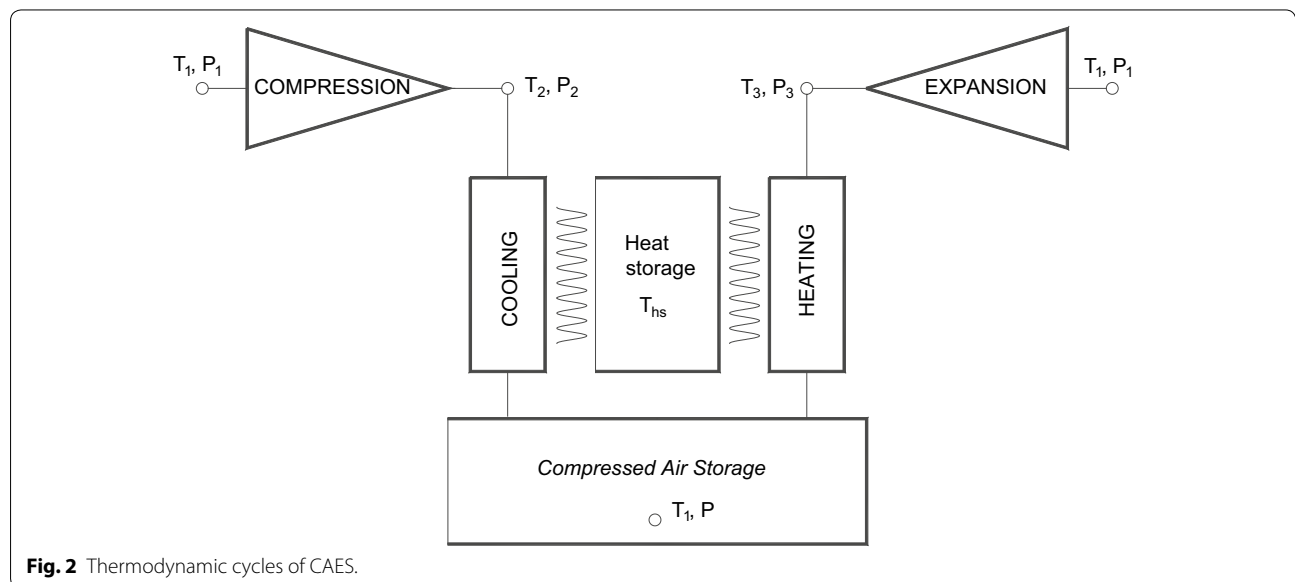


Fig. 2 Thermodynamic cycles of CAES.

where \dot{n} is the rate of air flow through the compressor (mol/s), and η_1 is the compression efficiency. The amount of air accumulated in the storage medium can be expressed as a function of compression time (t):

$$\dot{n} = (n_s - n_{s,i})/t_{in} = \dot{w}_{in}\eta_1/3.5R(T_2 - T_1) \quad (4)$$

$$n_{s,i} = \rho_i V / \mu \quad (5)$$

where t is the compression time in second, $n_{s,i}$ is the initial amount of air in the medium at $t=0$, ρ_i and μ are the initial density and solar mass of the air, for which 1.2 kg/m³ and 0.029 kg/mol were used in this study, respectively, and V is the storage volume (m³). The adiabatic temperature to pressure relationship for the air can be expressed, as follows:

$$T_2 = CP_2^{2/7} \quad (6)$$

where C is a constant taken to be 10.89 K/Pa^{2/7}. By substituting Eq. (6) into Eq. (4), the amount of the stored air in the medium can be estimated, as follows:

$$n_s = \dot{w}_{in}\eta_1 t_{in}/3.5R(CP_2^{2/7} - T_1) + n_{s,i} \quad (7)$$

Based on the ideal gas equation, following relationship can be obtained:

$$n_s = P_2 V / RT_2 = VP_2^{5/7} / RC \quad (8)$$

By using Eqs. (7) and (8), the pressure after compression (P_2) can be calculated, as follows:

$$VP_2^{5/7} / RC = \dot{w}_{in}\eta_1 t_{in}/3.5R(CP_2^{2/7} - T_1) + n_{s,i} \quad (9)$$

2.2.2 Cooling Process

In the cooling process, the high temperature of the compressed air resulted from the compression process (T_2) should be reduced approximately to its original temperature (T_1). The heat extracted from the air will be accumulated in a separated heat storage medium, such as oil, for the subsequent heating process before the expansion stage. There might be some heat loss during the heat extraction resulting in an efficiency, η_2 . The pressure and temperature relation at cooling and heating processes is assumed to be isochoric, and the heat extracted with zero work is directly proportional to the temperature change. Therefore, the temperature in the heat storage medium (T_{hs}), storage temperature (T) and pressure (P) of the air can be determined, as follows:

$$T_{hs} = \eta_2(T_2 - T_1) \quad (10)$$

$$T = T_1 \quad (11)$$

$$P = n_s RT / V \quad (12)$$

2.2.3 Heating Process

During the heating process, the stored air absorbs the heat from the heat storage medium. Some heat may be dissipated from the heat storage medium resulting in an efficiency, η_3 . Both the temperature and pressure linearly increase in the heating process, and thus following relationships can be obtained based on the ideal gas law:

$$T_3 = \eta_3 T_{hs} \quad (13)$$

$$P_3 = n_s RT_3 / V \quad (14)$$

2.2.4 Expansion Process

The expansion process can be assumed to be the reverse of the compression process for a power generation with an efficiency, η_4 . The relation of time, pressure before expansion, and generated power is governed by Eq. (8), which can be modified by replacing η_1 with $1/\eta_4$, as follows:

$$VP_3^{5/7} / RC = \dot{w}_{out} t_{out} / 3.5R\eta_4(CP_3^{2/7} - T_1) + n_{s,i} \quad (15)$$

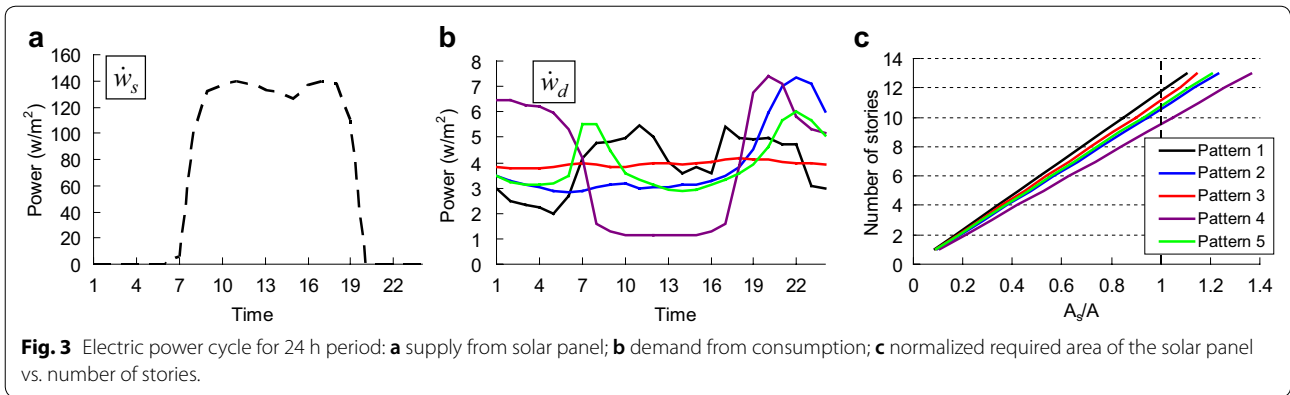
where \dot{w}_{out} is the power generated by the turbine. The total energy efficiency of the energy storage system can be expressed, as follows:

$$\eta_T = \dot{w}_{out} t_{out} / \dot{w}_{in} t_{in} = \eta_1 \cdot \eta_2 \cdot \eta_3 \cdot \eta_4 \quad (16)$$

3 Determination of the Air Pressure

3.1 Energy Supply and Demand

The renewable energy obtained from the solar panels is estimated from the field testing conducted by the National Laboratory of Astana (2017). An electricity power generated by solar photovoltaics (PV) panels installed in the Nazarbayev University for 24 h was measured by power inverters at meter stations, and a typical sunny day in the summer at the Astana was chosen to estimate the typical energy supply. Figure 3a shows the electricity power supply (\dot{w}_s) for 24 h period per square meter of the solar panel. A 24-h electricity power demand (\dot{w}_d) is obtained from the energy consumption data recorded from a typical residential apartment inside the Nazarbayev University provided by the University Service Management Department. The 24-h energy demand normalized by the residential area of the building is shown as the pattern 1 in Fig. 3b, and the total energy demand for 24 h was estimated to be 94.72 W/m². According to ArcGIS (2016), the average household size in Kazakhstan is 3.4 people per household, which typically occupies an approximate area of 75 m². Thus the annual household electricity power consumption can be estimated as $94.72 \times 75 \times 365/1000 = 2593$ kWh, which falls in the average range between 2000 and 3000 kWh for the household electricity power consumption for the



central Asia region reported in OVO Energy Ltd (2014). Four additional energy demand patterns are selected from Kwac et al. (2014) and those was scaled to be identical with the 24-h energy demand in the residential apartment, which shown in Fig. 3b as the patterns 2–5.

Energy surplus obtained by subtracting the energy demand from the energy supply between 7 a.m. to 7 p.m. is defined as the renewable energy available for the storage. This energy surplus can be used as the input power (\dot{w}_{in}) to go through the CAES cycles as expressed in Eqs. (1)–(16) of the previous section. Since the energy surplus also depends on the building floor area (A), the number of stories (N), and the area of the solar panel at the roof of the building (A_s), the input power can be computed using relationship between total energy supply and demand, as follows:

$$\dot{w}_{in} = \begin{cases} \dot{w}_s A_s - \dot{w}_d AN & \dot{w}_s A_s > \dot{w}_d AN \\ 0 & \dot{w}_s A_s \leq \dot{w}_d AN \end{cases} \quad (17)$$

Focusing on the cases, in which the total 24-h energy supply is just enough to cover the total 24-h energy demand, the energy balance equation can be derived, as follows:

$$\sum \eta_T \dot{w}_{in} + \sum \dot{w}_s A_s - \sum \dot{w}_{in} = \sum \dot{w}_d AN \quad (18)$$

Using Eq. (18) and the total energy efficiency for typical CAES cycles, i.e., $\eta_T = 0.75 \times 0.95 \times 0.95 \times 0.75 = 0.508$, as similarly observed in Elmegaard and Brixix(2011), the ratio between the solar panel area and building floor (A_s/A) can be plotted against the number of stories for the different demand patterns. As shown in Fig. 3c, the required area of the solar panel (A_s) increases with the number of stories (N) to achieve the energy balance from Eq. (18). When the number of stories is larger than 10, the required solar panel area (A_s) typically exceeds the available roof area (i.e., $A_s/A > 1.0$). Therefore, this paper

focuses on the residential building with the number of stories not more than 10.

3.2 Design of the Pile Foundation

The pile foundation is designed based on the current practice (Das 2010). Two key parameters were considered including the number of stories (N) and column spacing. The unfactored structural loads of each floor (i.e., the service loads) are estimated as 10 kPa for dead load and 3 kPa for live load, and thus the unfactored axial force of each column member can be calculated as: $N_{Ed} = (10 + 3)NA_{tr}$, where A_{tr} is the tributary area. A medium dense sand with $\gamma = 18$ kPa and $\phi' = 30^\circ$ is assumed for the pile foundation design. The strength of the pile foundation is provided from two main sources: the bearing capacity (Q_b) and the shaft friction capacity (Q_s), which can be determined following the procedures presented in Das (2010). The allowable stress design method was adopted in the pile foundation design, as follows:

$$N_{Ed}/n_p = N_p \leq Q_{all} = \min[(Q_b + Q_s)/2, (Q_b/3.5 + Q_s/1.5)] \quad (19)$$

where n_p is number of the piles for each column and N_p is the axial force of each pile. Using Eq. (19), the dimensions of the pile can be determined, and the design results are summarized in Table 1, where d_o and d_i are the outer and inner diameters for the pile, respectively, and L_p is the length of the pile. Noted that 1 m embedment depth is assumed for all the cases shown in Table 1.

The inner diameter (d_i) is significantly dependent on the strengths of the piles, and it governs the available energy storage volume inside the piles. The maximum allowable inner diameter can be calculated based on the allowable strength of the pile: $N_p \leq 0.25f_{ck}\pi(d_o^2 - d_i^2)/4$ as shown in the last column of Table 1, where f_{ck} is the characteristic strength of concrete, which was taken to be 25 MPa for C30 class concrete in this study.

Table 1 Design of the pile foundation.

N	N _{Ed} (kN)	n _p	N _p (kN)	d _o (m)	L _p (m)	Q _b (kN)	Q _s (kN)	Q _{all} (kN)	N _p /Q _{all}	Maximum d _i (m)
5 m × 5 m column spacing (A _{tr} = 25 m ²)										
2	650	1	650	1	6.5	1286	364	671	0.97	0.93
4	1300	2	650	1	6.5	1286	364	671	0.97	0.93
6	1950	3	650	1	6.5	1286	364	671	0.97	0.93
8	2600	3	867	1	9	1286	653	864	1.00	0.91
10	3250	3	1083	1	11.5	1286	1023	1111	0.98	0.88
6 m × 6 m column spacing (A _{tr} = 36 m ²)										
2	936	1	936	1	10	1286	791	956	0.98	0.90
4	1872	2	936	1	10	1286	791	956	0.98	0.90
6	2808	3	936	1	10	1286	791	956	0.98	0.90
8	3744	3	1248	1	13	1286	1285	1286	0.97	0.86
10	4680	4	1170	1	12.5	1286	1195	1225	0.96	0.87
7 m × 7 m column spacing (A _{tr} = 49 m ²)										
2	1274	2	637	1	6	1286	316	639	1.00	0.93
4	2548	3	849	1	9	1286	653	864	0.98	0.91
6	3822	4	956	1	10	1286	791	956	1.00	0.90
8	5096	4	1274	1	13	1286	1285	1286	0.99	0.86
10	6370	4	1593	1	16.5	1286	1971	1628	0.98	0.82

3.3 Calculation of Storage Pressure

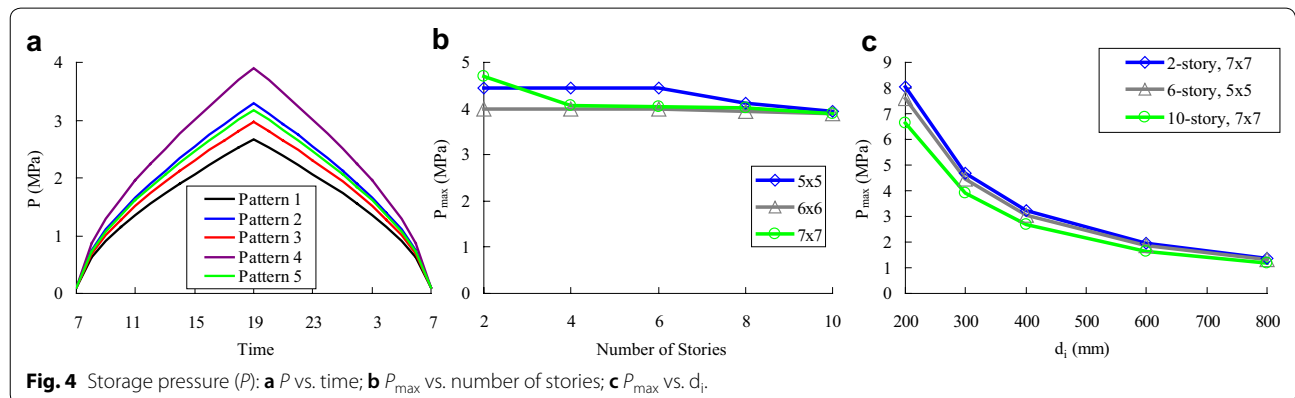
The available volume (*V*) of the CAES pile is determined from the dimensional details of the RC piles. The volume for the energy storage can be calculated, as follows:

$$V = n_p(L_p - 1.5)\pi d_i^2 / 4 \tag{20}$$

Based on the thermodynamic cycles presented in Sect. 2, the pressure (*P*₂) after compression process was first solved at different time (*t*_{in}) by inserting the input energy (*w*_{in}) and the available storage volume (*V*) obtained from Eq. (17) and Eq. (20), respectively, into Eq. (9). The temperature (*T*₂) after compression process can then be calculated using Eq. (6). After obtaining

*T*₂, the storage pressure (*P*) can be found using Eqs. (10 to 12). The calculated storage pressure (*P*) is shown in Fig. 4.

Figure 4a shows the estimated storage pressure (*P*) during a daily cycle from 7 a.m. to 7 a.m. of the next day for the different energy demand patterns for the case of ten stories building (i.e., *N* = 10), column spacing of 6 m × 6 m and *d*_{*i*} = 400 mm. As can be seen, the storage pressure starts to increase at 7 a.m. when the solar energy becomes available, and it goes up to the maximum pressure (*P*_{max}) at 7 p.m. After 7 p.m., the storage pressure typically decreases to release the energy, and it goes back to the original pressure at 7 a.m. of the next day because the storage pressures were calculated based on the energy



balance principal as expressed in Eq. (18). Since the demand pattern 4 has the least energy consumption from 7 a.m. to 7 p.m. for which the solar energy is available as shown in Fig. 3b, this pattern resulted in the highest pressure among all other five demand patterns. Therefore the demand pattern 4 can be considered as the most extreme case among the five demand patterns considered, and therefore, the energy demand pattern 4 was chosen for the analytical study.

Figure 4b shows the estimated maximum storage pressure (P_{max}) vs. the number of stories for different column spacing, in which the inner diameters for the pile (d_i) was set to be 300 mm for all the cases. As mentioned previously, the maximum storage pressures (P_{max}) were calculated using the energy demand pattern 4. The building with more number of stories and larger column spacing have more energy consumption, which results in more energy demands for the storage (w_{in}) to keep the total energy demand and supply equal for the 24 h period. However, at the same time, the taller building and larger column spacing requires more number of piles and longer pile length, which consequently results in more available storage volume (V). Therefore, as shown in Fig. 4b, it appeared that the maximum storage pressure (P_{max}) is not sensitive depending on the number of stories and column spacing.

Three cases with relatively higher P_{max} are selected for the finite element simulations including: 10-story building with 7 m × 7 m spacing; 6-story building with 5 m × 5 m spacing; 2-story building with 7 m × 7 m spacing. The maximum pressure distributions (P_{max}) of these three cases are compared in Fig. 4c against different inner pile diameter (d_i). The maximum pressures (P_{max}) clearly showed decrease trends as the inner diameter (d_i) increases, and this is surely because the available volume

increases for the energy storage as the inner diameter (d_i) increases.

4 Analytical Models

The concrete pile foundation was modeled using 3D solid elements as shown in Fig. 5, and the finite element models were built in the commercial finite element (FE) software ANSYS. Both the ends regions (0.5 m from the top and 1.0 m from the bottom) of the pile are modeled to be solid sections, and the middle part of the pile has hollowed sections. Two cases are considered for modeling of the concrete: the elastic and inelastic material models. The modulus of elasticity and Poisson ratio of C30 concrete were taken to be 31 GPa and 0.2, respectively, in the elastic FE model. For the inelastic analyses, the smeared crack approach was adopted to model the concrete and hoop reinforcement (Pramono and Willam 1989). The structural load (N_p) is applied as a uniformly distributed load at the top of the pile and the maximum inner pressure (P_{max}) was applied using the surface pressures at the inner surface of the pile model.

The soil-structure interaction was modeled in a simplified manner by using discrete contact elements, similar as the modeling approach used in Wan et al. (2015) and Zhang et al. (2016). The shaft friction (f) and soil lateral pressure (P_o) were introduced in the analysis through the discrete point-to-point contact element, so that the contact element can couple the behavior between the lateral pressure and the shaft friction. The input modeling parameters for the contact element include the normal stiffness (k_N), shear stiffness (k_s), coefficient of friction (μ_s) and initial gap (g_o). The normal stiffness (k_N) was calculated as the secant stiffness at half of the ultimate pressure (P_{0ult}) from the soil lateral response curve shown in Fig. 6a. The curve was developed based on the API

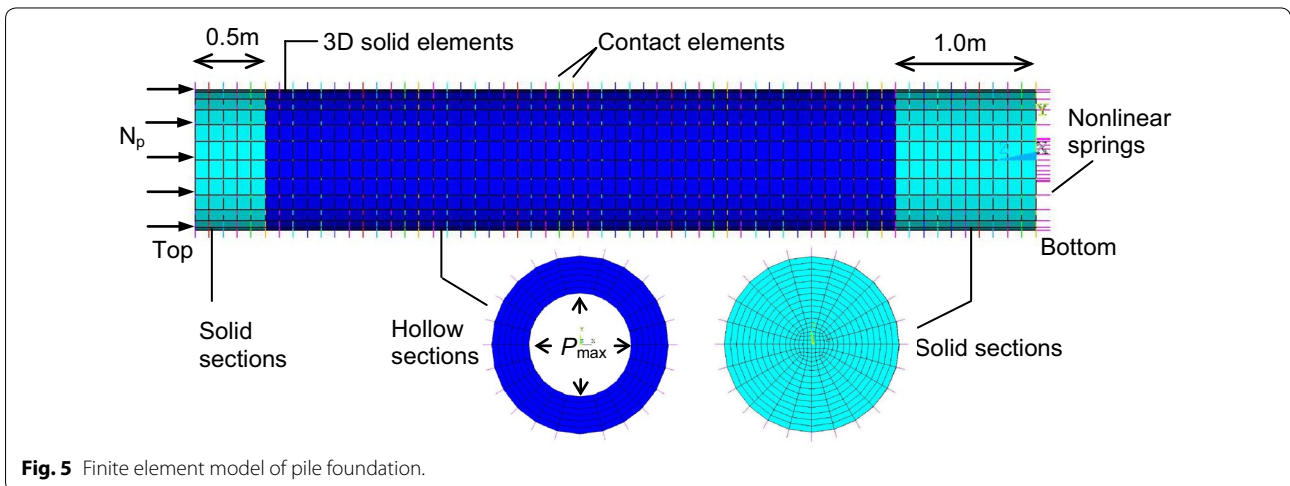
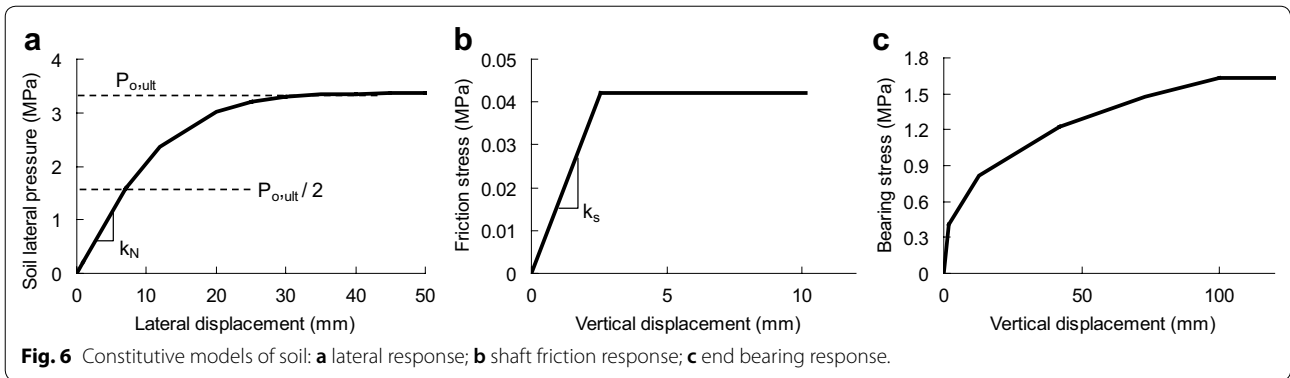


Fig. 5 Finite element model of pile foundation.



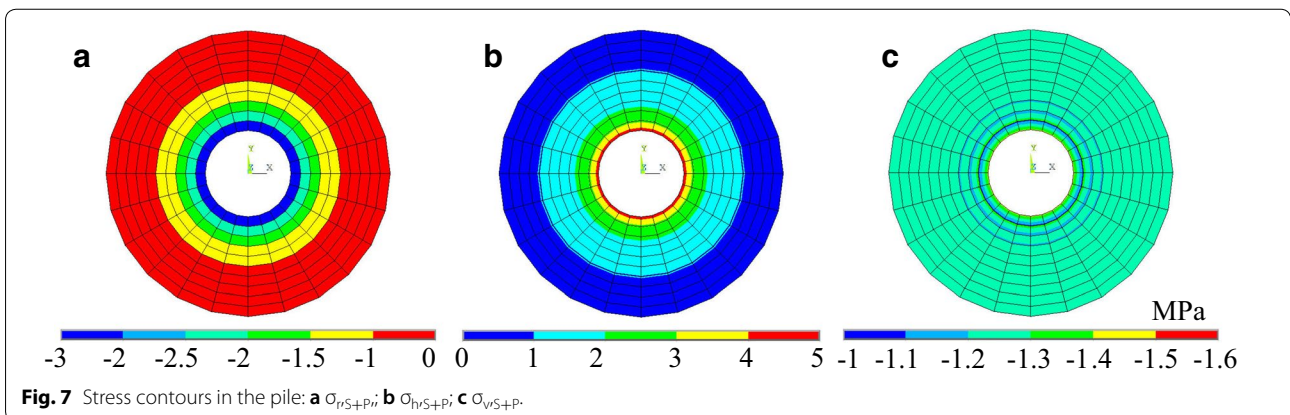
method (Brodbak et al. 2009; API 2002). The shear stiffness (k_s) was determined from the simplified soil friction response curve shown in Fig. 6b, which was developed by Loehr and Brown (2008). The coefficient of friction was taken to be $\mu = \tan(\phi' - 5^\circ)$. The initial gap (g_o) was also considered to provide the initial soil pressure applied on the pile, which can be calculated as $g_o = (1 - \sin\phi') \gamma z / k_N$, where z is the distance from the ground level. Since the friction (f) and lateral pressure (P_o) of the soil increase with the depth, the values of k_N , k_s and g_o varies with the depth (z). The end bearing (B) is modeled using nonlinear springs. The material properties of the nonlinear spring were determined from the simplified soil bearing response curve shown in Fig. 6c, which was presented by Loehr and Brown (2008). It should be noted that the pressure and stress values in Fig. 6 need to be multiplied by the tributary area of each discrete element when inputting them into the model.

5 Analytical Results

5.1 General Response from Elastic Analyses

The elastic analyses were conducted in the following steps: (1) applying the initial soil lateral pressure using the initial gap (g_o) in the contact element; (2) applying

the structural load (N_p); and (3) applying maximum air pressure (P_{max}) at the inner surface of the pile. In order to isolate the effect of the air pressure from the structural load (N_p) and soil boundary forces (f , B and P_o), the additional analyses were also conducted by applying the maximum air pressure (P_{max}) to the pile model without the contact and spring elements. Three load combination cases were considered to evaluate the critical stress distributions in the pile section: the structural load plus the soil boundary forces (S loading), the air pressure only (P loading), the combined structural load, the soil boundary forces and the air pressure (S+P loading). The general structural response was first examined for the 10-story building with $7\text{ m} \times 7\text{ m}$ column spacing, $L_p = 16.5\text{ m}$, $d_i = 300\text{ mm}$ ($r_i = 150\text{ mm}$), $P_{max} = 3.9\text{ MPa}$, and $N_p = 1593\text{ kN}$. Figure 7 shows the stress distributions in the radial, circumferential and vertical directions (σ_r , σ_θ and σ_v) at the middle of the pile ($z = 9.5\text{ m}$) under the S+P loading condition. Tensile stresses are clearly observed in the circumferential direction, while compression stresses are developed in the radial and vertical directions. The stress distribution is uniform along the circumferential direction, but



it varies along the radius (r) especially for the radial and circumferential stresses.

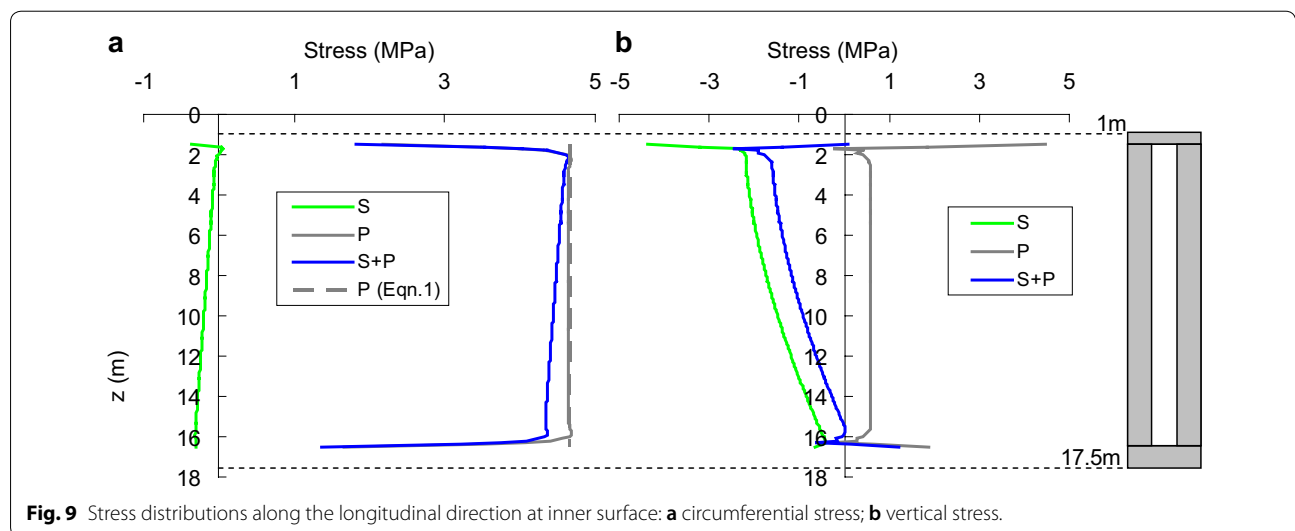
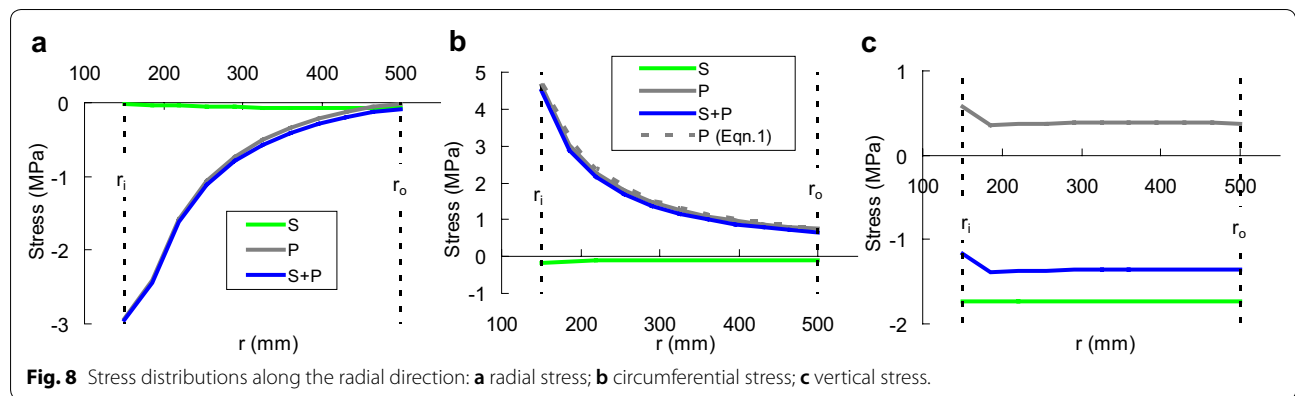
5.2 Stress Distribution along Radial Direction

Figure 8 shows the radial, circumferential and vertical stress distributions along the radial direction from the inner surface (r_i) to outer skin (r_o) at the middle of the pile length ($z=9.5$ m). As shown in Fig. 8a, the radial stresses are mainly induced from the air pressure, and it decreases from the inner surface to the outer. The radial stress from both the S and P loadings make the section in compression, but the magnitude is much smaller than the concrete compressive strength (25 MPa). Thus the radial stresses might not cause a structural safety issue for the pile foundation. As seen in Fig. 8b, the circumferential stress is also dominated by the air pressure, and it decreases from the inner surface to the outer. The circumferential stress from the S + P loading induces significant tensile stresses in the section, which clearly exceeds the tensile strength of concrete. The circumferential

stress obtained from the closed-form solution in Eq. (1) is also compared in Fig. 8b as dashed lines. The finite element solutions agrees well with the theoretical solutions. As shown in Fig. 8c, the compressive stresses are observed under the S loading, while the tensile stresses are observed under the P loading in the vertical direction. The tensile stresses from the P loading are much less than the compressive stress from the S loading, which finally results in the net compressive stresses from the S + P loading at $z=9.5$ m for this 10-story building. Also noted that the distribution of the vertical stresses along the radial direction are nearly uniform.

5.3 Stress Distribution along Longitudinal Direction

Figure 9 shows the circumferential and vertical stress distributions along the longitudinal direction of the pile (z) at the inner surface of the hollowed pile section. As can be seen in the Fig. 9a, the circumferential stress distribution from the P loading along the depth is nearly uniform except that the disturbed regions (the so-called D region)

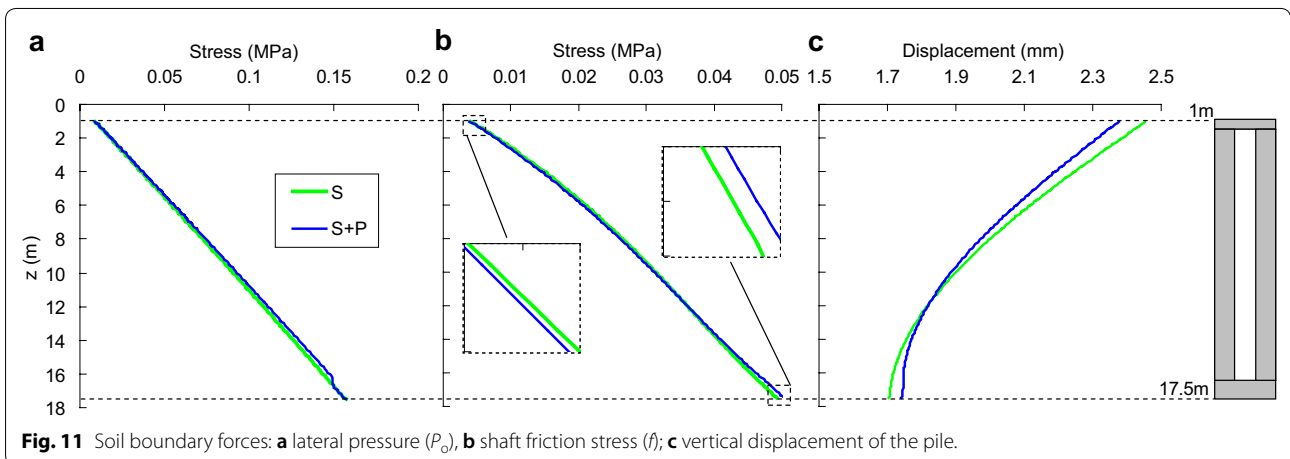
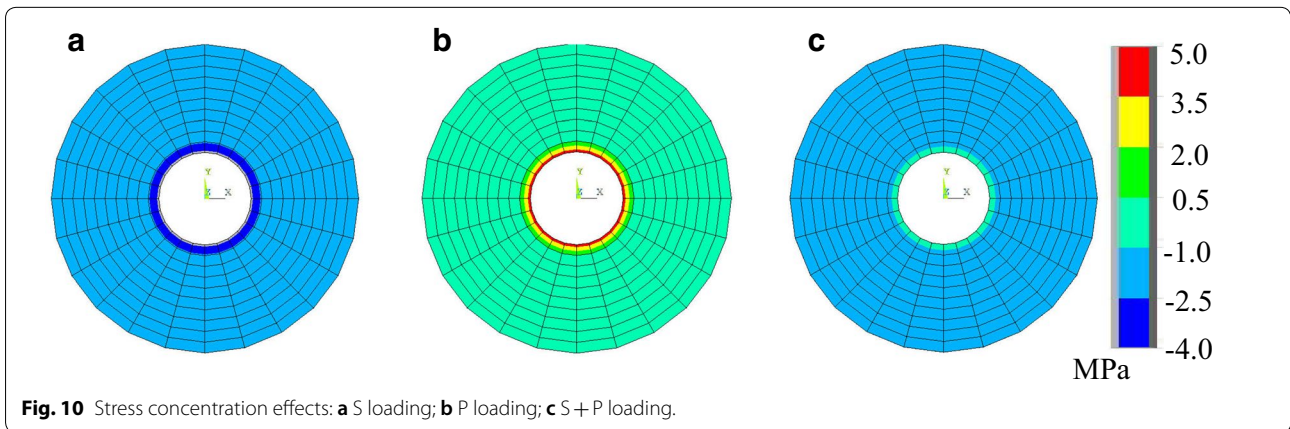


near the solid section shows smaller stress possibly due to stress concentration effects. The circumferential stress from the S loading slightly increases in compression with the increase of z due to the increase of the soil lateral pressure. This variation causes the circumferential stress from the S+P loading slightly higher near the top of the pile compared to the bottom. As shown Fig. 9b, except for the regions near the solid section, the vertical tensile stress from the P loading is constant along the depth, while the vertical compression induced from the S loading shows a decrease trend along the depth due to the presence of the shaft friction. Under the combined loading (S+P), the vertical stress starts with compression and gradually reduces along the depth (z), so that tensile stresses are finally observed near the bottom of the pile (e.g. $z \approx 16$ m). For the regions near the solid section, as mentioned before, the stress concentrations can be observed due to a sharp transition of the section shape from the hollowed to solid sections. The stress concentration occurs at the inner surface of the pile as shown in Fig. 10, and it results in the high compressive stress under

the S loading and high tensile stress under the P loading. Therefore, the S+P loading shows less severe stress concentration effects as shown in Figs. 9b and 10c. This stress concentration effect might be exaggerated in the numerical solution, and it can be significantly relieved by a smooth section transition between the hollowed and solid sections.

5.4 Soil-Structural Interaction

Figure 11 shows the soil boundary forces (P_o and f) and the vertical displacement distributions of the pile under the S loading and S+P loading. It appears that the air pressure has marginal effects on the soil boundary forces because the changes in the soil lateral pressure and the shaft friction stress are not significant between the S and S+P loadings as shown in Figs. 11a, b. The soil lateral pressure increases slightly due to the lateral expansion of the pile under the air pressure as shown in Fig. 11a. As shown in Fig. 11b, the air pressure slightly decreases the shaft friction stress for the region where z is less than 11 m, while the shaft friction stress increases due to



the air pressure when z is larger than 11 m. This trend is because the air pressure elongates the pile along the z direction, and it can result in decrease of the vertical displacement in the upper part of the pile but increase of the vertical displacement in the lower part as shown in Fig. 11c. In addition, the shaft friction stress is directly proportional to the vertical displacement as shown in Fig. 6b, thus the shaft friction stresses decreases first and then increases again along the depth (z).

5.5 Parametric Results

Figure 12 shows the circumferential and vertical stress distributions of the pile section in the 10-story and $7\text{ m} \times 7\text{ m}$ column spacing under the S+P loading with different inner radius (r_i). The circumferential stresses are taken at the depth where maximum value is observed near the top of pile as indicated in Fig. 9b. For the vertical stresses, the average stress values along the radial direction at each depth (z) are used in Fig. 12b to eliminate the unrealistic stress concentration. As shown in Fig. 12a, the circumferential stress shows the similar distribution trend from the inner to the outer surfaces for different inner radius (r_i). The stress variations are larger for the piles with smaller inner radius (r_i), while the stress are distributed more uniformly for the cases with large radius (r_i). The maximum circumferential stress decreases up to the case with 300 mm of the radius, because the applied air pressure (P_{\max}) decreases when the radius increases (Refer to Fig. 4c), so that the maximum circumferential stress also decreases. However, when the inner radius (r_i) is larger than 300 mm, at this threshold value, the thickness of hollowed pile section is small enough to increase the circumferential stress again. As shown in Fig. 12b,

the vertical stress, which is in compression at the top but in tension at the bottom, increases in magnitude as the inner radius (r_i) increases.

The maximum tensile stresses observed in the pile section for the three selected cases with different numbers of stories (N) are evaluated under the S+P loading case. Figure 13 shows the distributions of the maximum tensile stress according to the inner radius (r_i) for $N=2, 6$ and 10. The tensile strength of the C30 concrete ($f_{ctm}=2.6\text{ MPa}$) is also indicated as dashed horizontal line in Fig. 13. As shown in Fig. 13a, the maximum circumferential stress at the inner surface initially decreases to the certain point and then increases as the inner radius (r_i) increases, which is consistent with the trend shown in Fig. 12a. At the outer surfaces, the circumferential stresses continuously increase as the inner radius (r_i) increases. As the number of stories increases, the circumferential stresses shows a decrease trend, which is consistent with the variation of the air pressure (P_{\max}) as shown in Fig. 4c. As shown in Fig. 13b, the maximum tensile vertical stress decreases as the inner radius decreases, and it eventually shows compressive stresses at $r_i=100\text{ mm}$. However, except for $r_i=400\text{ mm}$, the tensile stress is negligible compared to the tensile strength of concrete (f_{ctm}). As indicated in Fig. 13a, the maximum circumferential stress at inner surface is quite larger than the tensile strength of concrete (f_{ctm}) for all the cases, which means that the cracked concrete section is expected in the service load combined with the air pressure (P_{\max}).

However, except for the case with $r_i=400\text{ mm}$, the maximum circumferential stresses at the outer surface are smaller than the tensile strength of concrete (f_{ctm}), so that the partially cracked section can be utilized in the serviceability design. In this situation, the hoop

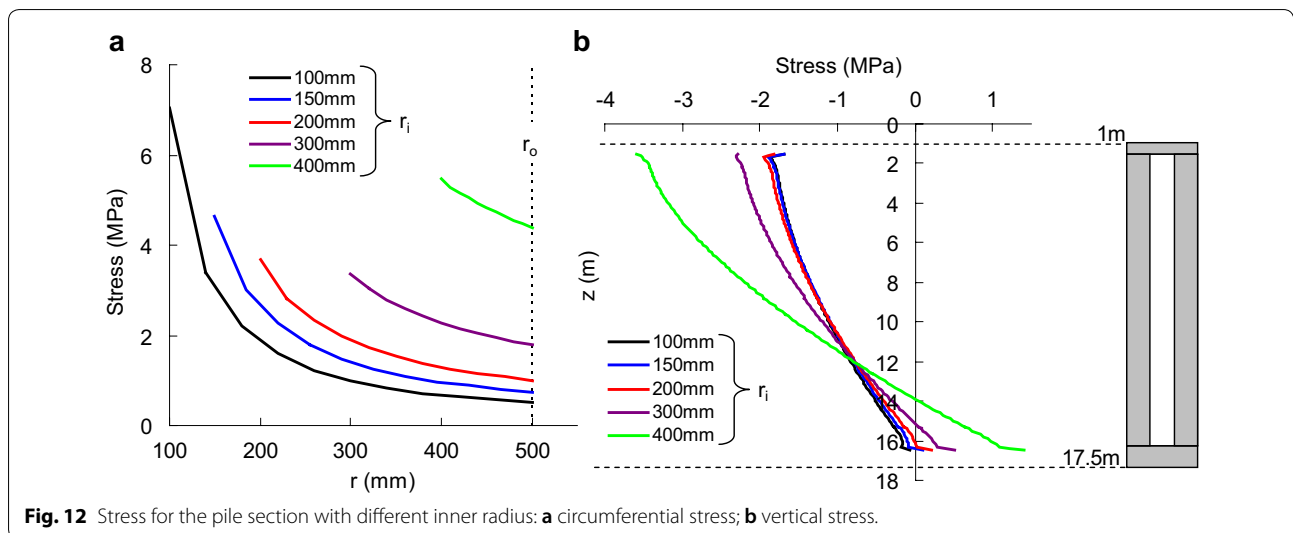


Fig. 12 Stress for the pile section with different inner radius: **a** circumferential stress; **b** vertical stress.

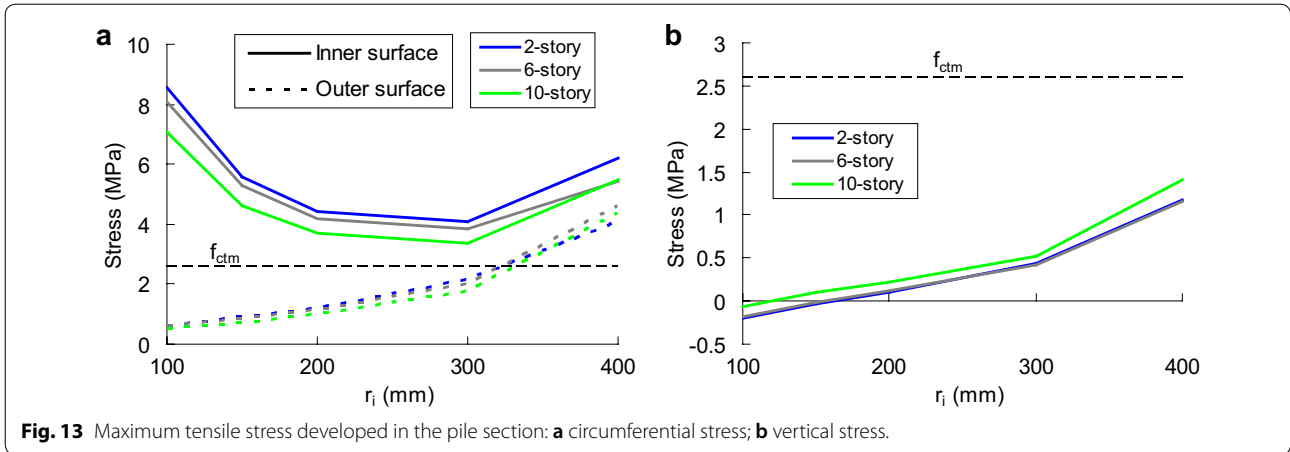


Fig. 13 Maximum tensile stress developed in the pile section: **a** circumferential stress; **b** vertical stress.

reinforcements can be introduced to control and compensate the tensile stresses induced in the hollowed pile section. The minimum required hoop reinforcements can be provided to resist the maximum circumferential stress at the inner surface ($f_{t,in}$) shown Fig. 13a, as follows:

$$A_{st,min}f_s = A_c f_{t,in} \tag{21}$$

where $A_{st,min}$ is the minimum required area of the hoop reinforcement, f_s is the allowable stress of the hoop reinforcement, which can be taken to be 60% of the yield strength of hoop reinforcement according to the ACI318 (Bektimirova et al. 2017) for the serviceability design, (e.g., for Grade 500 MPa, $f_s = 0.6 \times 500 = 300$ MPa), and A_c is the gross area of the concrete section. However, the provided minimum hoop reinforcements cannot fully prevent the crack penetration throughout the entire section, because the concrete cracking strain (f_{ctm}/E_c) is quite smaller than the strain corresponding to the allowable stress of the hoop reinforcement (f_s/E_s). To this end, the stress of the hoop reinforcement at the concrete cracking ($f_{s,ck}$) can be calculated based on the strain compatibility, as follows:

$$f_{s,ck} = E_s f_{ctm} / E_c \tag{22}$$

where E_s is the modulus elasticity of the steel, which can be taken as 200 GPa. For the concrete considered in this paper, $f_{s,ck}$ is equal to 16.8 MPa (i.e.,

$200/31 \times 2.6 = 16.8$ MPa). To prevent the crack penetration through the entire section, the required amount of the hoop reinforcements ($A_{st,max}$) can be conservatively calculated by ignoring the contribution of concrete, as follows:

$$A_{st,max}f_{s,ck} = A_c f_{t,out} \tag{23}$$

where $f_{t,out}$ is the maximum circumferential stress at the outer surface shown in Fig. 13a. Based on Eq. (23), the minimum and maximum circumferential reinforcement ratios can be derived, as follows:

$$\rho_{h,min} = A_{st,min} / A_c \tag{24}$$

$$\rho_{h,max} = A_{st,max} / A_c \tag{25}$$

Table 2 shows the required hoop reinforcement ratios estimated from Eqs. (24) and (25) for different cases. It should be noted that the cases with $r_i = 300$ mm and $r_i = 400$ mm were excluded because their maximum circumferential stresses at the outer surface ($f_{t,out}$) are very close to or exceeds the cracking stress of concrete (f_{ctm}).

5.6 Nonlinear Analyses

The nonlinear analyses were conducted using the inelastic constitutive models, in which the various reinforcement ratios ranged from $\rho_{h,min}$ to $\rho_{h,max}$ shown in Table 2 were considered to validate the proposed hoop

Table 2 Circular reinforcement ratio.

r_i (mm)	$f_{t,out}$ (Mpa)			$\rho_{h,min}$			$f_{t,in}$ (Mpa)			$\rho_{h,max}$		
	N=2	N=6	N=10	N=2 (%)	N=6 (%)	N=10 (%)	N=2	N=6	N=10	N=2 (%)	N=6 (%)	N=10 (%)
100	8.57	8.10	7.05	2.9	2.7	2.3	0.64	0.60	0.52	3.8	3.6	3.1
150	5.58	5.28	4.64	1.9	1.8	1.5	0.90	0.85	0.74	5.4	5.1	4.4
200	4.42	4.19	3.69	1.5	1.4	1.2	1.20	1.14	1.00	7.2	6.8	6.0

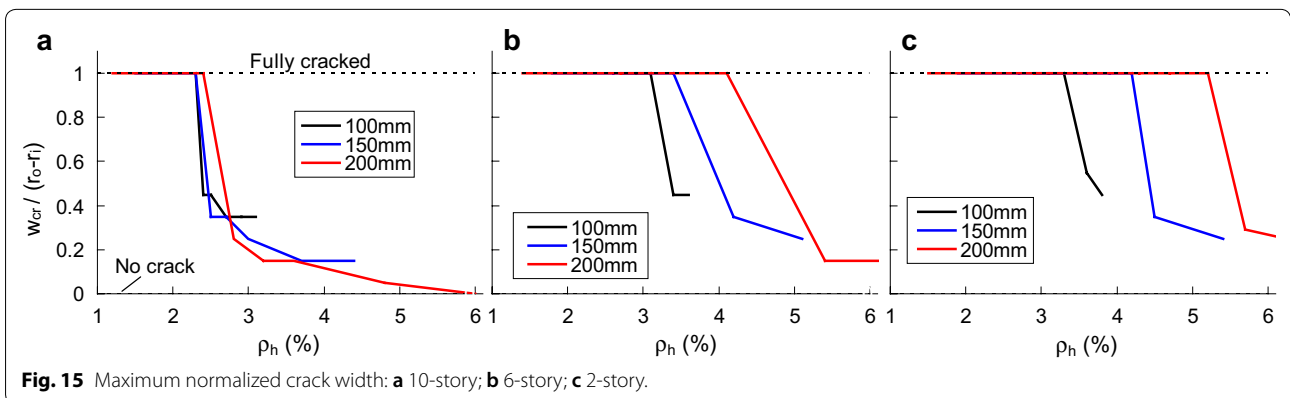
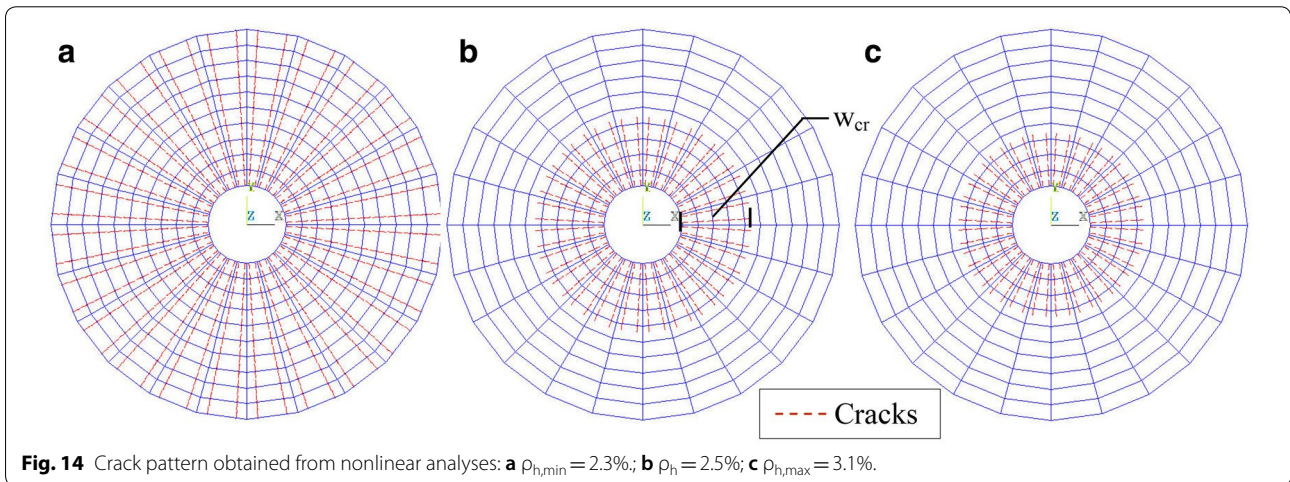
reinforcement ratios expressed in Eqs. (24) and (25). In the finite element models, 1.0% longitudinal reinforcement ratio was considered according to the typical design practices. Figure 14 shows the crack patterns at the critical section near the top of the pile for the case with 10 stories and $r_i=100$ mm, and the crack distributions are uniform in the circumferential direction. It appears that the radial crack fully penetrates through the pile section, if only the minimum hoop reinforcement is provided ($\rho_{h,min}=2.3\%$). On the other hand, at the maximum hoop reinforcement ratio ($\rho_{h,max}=3.1\%$), as shown Fig. 14c, about 35% of the concrete section are cracked.

Figure 15 shows the maximum crack width (w_{cr}) estimated from the nonlinear analyses against the hoop reinforcement ratios ranged from $\rho_{h,min}$ to $\rho_{h,max}$ for all the cases shown in Table 2. The crack widths are normalized by the thickness of the pile section (r_o-r_i), which serves as the percentage indicator of the crack penetration behaviors. As shown in Fig. 15, all the cases reinforced with the minimum hoop reinforcement are fully cracked. For the cases with the maximum hoop reinforcement ratios, the

cracks partially penetrate within some parts of the pile sections. As indicated in Fig. 15, in order to prevent fully cracked sections under the service loads, the sufficient amounts of the hoop reinforcements have to be provided for different cases. As the inner radius (r_i) increases, the required hoop reinforcement ratio significantly increases to prevent fully cracked section, and it is estimated to be more than 4.0%, which is greater than the maximum shear reinforcement ratio specified in ACI318 (2008). On this basis, only the cases with $r_i=100$ mm can be practically used considering the reasonable hoop reinforcement ratios ranged from 2.5 to 3.5%, as shown in Fig. 15.

6 Conclusions

This paper presents the structural responses of the proposed energy storage pile foundation under the combined structural loading, soil effects and compressed air pressure. The magnitude of the air pressure was determined from the thermodynamic cycles of the CAES based on the available renewable energy for storage, the corresponding building geometries and pile foundation



dimensions. The detailed parametric analyses were conducted using the finite element approach to examine the critical tensile stress and the crack pattern in the energy storage pile foundation. On this basis, following conclusions can be drawn:

1. The storage pressure shows no significant change depending on the number of stories and column spacing, because the available energy and storage volume can be proportionally matched. However, it appears that the compressed air pressure highly depends on the energy demand patterns and the inner diameter of the pile foundation.
2. The proposed energy storage pile foundation is suitable for buildings with 10 stories or less because there might not be sufficient renewable energy to be stored for buildings with more than 10 stories.
3. The combined structural loads and air pressures can result in the significant circumferential tensile stresses and radial cracks in the pile section with the normal strength concrete. These circumferential stresses show the non-uniform distribution along the radial direction of the pile section. The maximum stresses are higher in the inner surface and gradually reduces to the outer surface.
4. The combined structural loading and high pressure induce the tensile stresses in the longitudinal direction near the bottom of the pile in some cases, where the air pressure is high enough to overcome the effect of the vertical compression load. However, it clearly appears that these tensile stresses are less than the tensile strength for the normal strength concrete.
5. The pressure induced from the energy storage in the form of the compressed air can reduce the shaft friction in the upper portion of the pile but can increase the shaft friction in the lower portion. However, the influence of the air pressure on the shaft friction is marginal.
6. The crack patterns along the circumferential direction are almost uniformly distributed in the pile section, but the hoop reinforcements are surely required to prevent and control the crack penetration through the entire pile section. The minimum and maximum circumferential reinforcement ratios are also proposed for the proper crack control in the design of the energy storage pile foundation.
7. For the designs of the conventional RC CAES pile with the normal strength concrete, small inner diameter is preferred to have a practical and economical design reinforcement ratios. For the cases studied in this paper, the required hoop reinforcement ratios are ranged from 2.5 to 3.5% to prevent the fully-cracked section in the service load level.

It is also noticed that cracking damage is unavoidable for the conventional RC CASE pile under daily service loads. Moreover to prevent possible energy leakage, relative high degree of the hoop reinforcement ratio (2.5–3.5%) is required, which might cause congestion of the reinforcement inside the pile foundation. Therefore, alternative solutions can be further explored for the CASE pile to prevent the service level cracking including (1) adopting ultra high performance concrete (Bektimirova et al. 2017); and (2) using double-tube steel pile with concrete infills (Agibayeva et al. 2018).

7 Abbreviations

CAES, compressed air energy storage; RC, reinforced concrete; PV, photovoltaics.

7.1 List of Symbols

A , building floor area; A_c , concrete cross-section area in the pile section; A_s , area of the solar panels; $A_{st,min}$, $A_{st,max}$, minimum, maximum hoop reinforcement area; A_{tr} , tributary area to the column; B , end bearing; C , adiabatic constant; d_i , d_o , inner, outer diameter of the pile section; E_s , E_c , Young's modulus for reinforcement, concrete; f , shaft friction between the soil and the pile; f_{ck} , f_{ctm} , concrete compression, tension strength; $f_{s,ck}$, working stress in the reinforcement at the verge of concrete cracking; $f_{t,in}$, $f_{t,out}$, maximum circumferential stress at inner, outer surface; g_o , and initial gap; k_N , k_s , normal, shear stiffness of the contact element; L_p , length of pile; N , number of stories; N_{Ed} , unfactored axial force on each column; N_p , axial force on each pile; n , amount of air; \dot{n} , rate of the air flow; n_p , number of the piles per column; $n_{s,i}$, initial amount of air in storage tank at $t=0$; P , inner pressure from the compressed air; P_1 , ambient air pressure; P_2 , P_3 , compressed air pressure before, after cooling; P_{max} , maximum air pressure in the pile foundation; P_o , soil lateral pressure; $P_{o,ult}$, ultimate lateral pressure; Q_{all} , allowable bearing capacity; Q_b , Q_s , end bearing, shaft friction capacity; R , universal gas constant; r , radius along the thickness of the pile section; r_i , r_o , inner, outer radius of the pile section; T , absolute air temperature; T_1 , absolute ambient air temperature; T_2 , T_3 , absolute compressed air temperature before, after cooling; T_{hs} , temperature in the heat storage medium; t_{in} , compression time; t_{out} , expansion time; V , storage volume; w , work done by the air; w_{cr} , crack width; w_{in} , w_{s} , power demand, supply per hour; \dot{w}_{in} , electric power from solar panel; \dot{w}_{out} , electric power generated by turbine; z , soil depth measured from the ground. ϕ' , soil friction angle; γ , unit weight of the soil; η_1 , compression efficiency; η_2 , heat extraction efficiency; η_3 , heat storage efficiency; η_t , turbine efficiency; η_T , system total efficiency; μ , molar mass of the air; μ_s , coefficient of friction; ρ_p , hoop reinforcement ratio; $\rho_{h,min}$, $\rho_{h,max}$, minimum and

maximum hoop reinforcement ratios; ρ_i , ambient air density; $\sigma_{h,p}$, circumferential stress under inner air pressure; $\sigma_{h,s}$, circumferential stress under structural loads and soil boundary forces; $\sigma_{r,p}$, radial stress under inner air pressure; $\sigma_{r,s}$, radial stress under structural loads and soil boundary forces; $\sigma_{v,p}$, vertical stress under inner air pressure; $\sigma_{v,s}$, vertical stress under structural loads and soil boundary forces; $\sigma_{h,s+p}$, circumferential stress under the combined loads; $\sigma_{r,s+p}$, radial stress under the combined loads; $\sigma_{v,s+p}$, vertical stress under the combined loads.

Authors' contributions

The manuscript has the following novelty contributions: a new renewable energy storage foundation system was proposed. The required storage pressure for the energy storage pile was evaluated through thermodynamic analyses. The maximum tensile stresses in the pile foundation were investigated through elastic finite element analyses. Crack patterns of the pile foundation were examined through inelastic finite element analyses. Design recommendations for the energy storage foundation system were made. All authors read and approved the final manuscript.

Acknowledgements

The authors would like to thank the National Laboratory of Astana to provide the solar energy generation data and the University Service Management Department at Nazarbayev University to provide the electric power consumption data.

Competing interests

The authors declare that they have no competing interests.

Availability of data and materials

Not applicable.

Consent for publication

The manuscript is being submitted for *International Journal of Concrete Structures and Materials*.

Ethics approval and consent to participate

The authors confirm that the manuscript has been read and approved by all named authors and that there are no other persons who satisfied the criteria for authorship but are not listed. The authors further confirm that the order of authors listed in the manuscript has been approved by all the authors.

Funding

This research was supported by the Nazarbayev University Research Fund under Grant (#SOE2017001) "Development of a Renewable Energy Storage System using Reinforced Concrete Foundations". The authors are grateful for this support. Any opinions, findings, and conclusions or recommendations expressed in this material are those of the author(s) and do not necessarily reflect the views of the Nazarbayev University.

Publisher's Note

Springer Nature remains neutral with regard to jurisdictional claims in published maps and institutional affiliations.

Received: 30 January 2018 Accepted: 4 July 2018

Published online: 27 November 2018

References

ACI318-08 (2008). *Building code requirements for structural concrete and commentary*, ACI committee 318.

- ACI350 (2014). *Code requirements for environmental engineering concrete structures*. American Concrete Institute Committee 350.
- Agibayeva, A., Ju, H., Zhang, D., Moon, S. W., Kim, J., & Lee, D. H. (2018). Application of CFT pile foundation as an energy storage media, joint nu-snu mini-symposium on the design and analysis of innovative structural and geotechnical systems. *The 2018 International Conference on advances in computational design*, August 28–31, Incheon, South Korea.
- Al Shemmeri, T. (2010). *Engineering thermodynamics*. Tarik Al-Shemmeri & Ventus Publishing ApS.
- API (2002). *Recommended practice for planning, designing and constructing fixed offshore platforms—working stress design*. API recommended practice report 2A-WSD. American Petroleum Institute, December.
- ArcGIS, Kazakhstan average household size (2016). Online report: <http://www.arcgis.com/home/item.html?id=f79fb6456d5e46e48df08a86685e6e5a>. Accessed 6 Mar 2017.
- Azabi, T. (2014). *Behaviour of reinforced concrete conical tanks under hydrostatic loading*, Master Thesis, the University of Western Ontario.
- Bektimirova, U., Tleuken, A., Satekenova, E., Shon, C., Zhang, D., & Kim, J. (2017). Preliminary experimental investigation on the strength and air permeability of reactive powder concrete. *6th International Conference on material science and engineering technology*, Seoul, Republic of Korea, October 20–22.
- Brodbak, K., Moller, M., Sorensen, S., & Augustesen, A. (2009). *Review of p-y relationships in cohesionless soil*. DCE Technical Reports No. 57, Aalborg University.
- Cavallo, A. (2007). Controllable and affordable utility-scale electricity from intermittent wind resources and compressed air energy storage (CAES). *Energy*, 32(2), 120–127.
- Das, B. (2010). *Principles of foundation engineering*. Boston: Cengage Learning.
- Elmegaard, E., & Brix, W. (2011). Efficiency of compressed air energy storage. In *24th International Conference on efficiency, cost, optimization, simulation and environmental impact of energy systems*.
- Energy Storage Association (2018). Compressed air energy storage. <http://energystorage.org/compressed-air-energy-storage-caes>. Accessed 8 Jan 2018.
- Hayter, S., & Kandt, A. (2011). *Renewable energy applications for existing buildings*. Technical Report NREL/CP-7A40-52172.
- Kwac, J., Flora, J., & Rajagopal, R. (2014). Household energy consumption segmentation using hourly data. *IEEE Transactions on Smart Grid*, 5(1), 420–430.
- Loehr, E., & Brown, D. (2008). *A method for predicting mobilization resistance for micropiles used in slope stabilization applications*. A report prepared for the joint ADSC/DFI Micropile Committee.
- Lund, H., & Salgi, G. (2017). The role of compressed air energy storage (CAES) in future sustainable energy systems. *Energy Conversion and Management*, 50(5), 1172–1179.
- National Lab Astana (2017). *Development and research of highly efficient solar cells based on various new semiconductor materials*. <https://nla.nu.edu.kz/en/ceams/rireesefe/laboratory-of-solar-energy>. Accessed 10 Apr 2017.
- OVO Energy Ltd (2014). *How much electricity does a home use?* <https://www.ovoenergy.com/guides/energy-guides/how-much-electricity-does-a-home-use.html>. Accessed 6 Mar 2017.
- Pramono, E., & Willam, K. (1989). Fracture energy-based plasticity formulation of plain concrete. *Journal of Engineering Mechanics*, 115(6), 711–1183.
- Purushothama, P., & Ramasamy, V. (2010). *Strength of materials, pearson education india*, 1st edition.
- Rugolo, J., & Aziz, M. (2012). Electricity storage for intermittent renewable sources. *Energy & Environmental Science*, 5(5), 7151–7160.
- Sabirova, A., Zhang, D., Kim, J., Nguyen, M., & Shon, C. (2016). Development of a reinforced concrete foundation system for renewable energy storage. *Proceedings of the 8th Asian Young geotechnical engineering conference*. Astana, Kazakhstan, August 5–7.
- Tulebekova, S., Saliyev, D., Zhang, D., Kim, J., Karabay, A., Turlybek, A., & Kazbayeva, L. (2017). Preliminary analytical study on the feasibility of using reinforced concrete pile foundations for renewable energy storage by compressed air energy storage technology. *Global Congress on Construction, Material and Structural Engineering*. Johor Bahru, Malaysia, August 27–28.

Wan, G., Zhang, D., Fleischman, R.B. and Naito, C.J. (2015) A coupled connector element for nonlinear static pushover analysis of precast concrete diaphragms. *Engineering Structures*, 86, 58–71.

Zhang, L., Ahmari, S., Sternberg, B., & Muniram, B. (2012). *Feasibility study of compressed air energy storage using steel pipe piles*. GeoCongress: State of the Art and Practice in Geotechnical Engineering.

Zhang, D., Fleischman, R., Naito, C.J. and Zhang, Z. (2016) Development of diaphragm connector elements for three-dimensional nonlinear dynamic analysis of precast concrete structures. *Advances in Structural Engineering*, 19(2), 187–202

Submit your manuscript to a SpringerOpen[®] journal and benefit from:

- ▶ Convenient online submission
- ▶ Rigorous peer review
- ▶ Open access: articles freely available online
- ▶ High visibility within the field
- ▶ Retaining the copyright to your article

Submit your next manuscript at ▶ [springeropen.com](https://www.springeropen.com)
